

Position Information from Reflecting Surfaces

Anastasios Kakkavas, *Student Member, IEEE*, Mario H. Castañeda García, *Member, IEEE*, Gonzalo Seco-Granados, *Senior Member, IEEE*, Henk Wymeersch, *Senior Member, IEEE*, Richard A. Stirling-Gallacher, *Member, IEEE*, and Josef A. Nossek, *Life Fellow, IEEE*

Abstract—In the context of positioning a target with a single-anchor, this contribution focuses on the Fisher information about the position, orientation and clock offset of the target provided by single-bounce reflections. The availability of prior knowledge of the target’s environment is taken into account via a prior distribution of the position of virtual anchors, and the rank, intensity and direction of provided information is studied. We show that when no prior knowledge is available, single-bounce reflections offer position information in the direction parallel to the reflecting surface, irrespective of the target’s and anchor’s locations. We provide a geometrically intuitive explanation of the results and present numerical examples demonstrating their potential implications.

Index Terms—positioning, localization, NLOS, reflection, single-bounce

I. INTRODUCTION

Although the majority of practical positioning systems rely heavily or even exclusively on line-of-sight (LOS) propagation, the role of non-LOS (NLOS) propagation in wireless positioning has been widely studied. Traditionally, the focus has been on the mitigation of the negative impact of NLOS paths on positioning accuracy [1], with some approaches completely disregarding NLOS links and others aiming to correct the NLOS-induced bias in the range estimate [2]. An alternative approach is to treat the NLOS paths as additional sources of position information. An early work in this direction was [3], where it was shown that given distance, angle of departure (AOD) and angle of arrival (AOA) measurements of a single-bounce NLOS path, the receiver (Rx) can lie on a line segment, and an algorithm exploiting this observation was presented. A similar approach for mobile targets was presented in [4].

This work was supported in part by the EU-H2020 project Fifth Generation Communication Automotive Research and Innovation (5GCAR), and in part by the ICREA Academia program and the Spanish Ministry of Science, Innovation and Universities project TEC2017-89925-R.

A. Kakkavas is with the Munich Research Center, Huawei Technologies Duesseldorf GmbH, 80992 Munich, Germany, and also with the Department of Electrical and Computer Engineering, Technical University of Munich, 80333 Munich, Germany (e-mail: anastasios.kakkavas@huawei.com).

M. H. Castañeda García and R. A. Stirling-Gallacher are with the Munich Research Center, Huawei Technologies Duesseldorf GmbH, 80992 Munich, Germany (e-mail: mario.castaneda@huawei.com; richard.sg@huawei.com).

G. Seco-Granados is with the Department of Telecommunications and Systems Engineering, Universitat Autònoma de Barcelona, Spain (UAB) (e-mail: gonzalo.seco@uab.cat).

H. Wymeersch is with the Department of Electrical Engineering, Chalmers University of Technology, 412 58 Gothenburg, Sweden (email: henkw@chalmers.se).

J. A. Nossek is with the Department of Electrical and Computer Engineering, Technical University of Munich, 80333 Munich, Germany (e-mail: josef.a.nossek@tum.de).

Such approaches became much more relevant for fifth generation (5G) networks [5]. The upcoming exploitation of the large chunks of available bandwidth at millimeter-wave (mm-Wave) frequencies and the use of antenna arrays with a large number of elements, enable the possibility of highly accurate temporal and angular measurements, and improve the separability of multipath components [6]. The increased temporal and angular resolution has made single-anchor positioning [7] an attractive option when links to multiple anchors may not be available. Algorithms for single-anchor localization and mapping with a single snapshot have been presented in [8], [9] and [10] among others. In [11] it was shown that, in a two-dimensional (2D) setup, the set of time of arrival (TOA), AOD and AOA measurements from a single-bounce reflection offers rank-1 information for a receiver with unknown position and orientation. The corresponding eigenvalue of the position and orientation equivalent FIM (EFIM) was computed analytically, showing that all 3 measurements are required for extracting additional position information from NLOS components. In [12] it was shown that single-bounce NLOS components can be helpful in resolving the clock offset between an imperfectly synchronized transmitter (Tx)-Rx pair, allowing for accurate single-anchor positioning.

In this letter, considering flat reflecting surfaces, which we refer to as reflectors, we extend the work of [3], as well as [11] and [12], as follows:

- We show that, when no prior information about the reflector is available, the direction of position information is parallel to the reflector and independent of the Tx and Rx position. Hence, the line segment where the receiver can lie given the measurements of a NLOS path, as identified in [3], is always orthogonal to the reflecting surface.
- By encoding prior information about reflectors as prior distribution of the location of their corresponding virtual anchors (VAs), we study the effect of the accuracy of prior information on the intensity and direction of position information offered by single-bounce reflections.

II. SYSTEM MODEL

A. System Model

The Tx consists of an array with N_T antennas and reference point located at $\mathbf{p}_T = [p_{T,x}, p_{T,y}]^T \in \mathbb{R}^2$, where $(\cdot)^T$ denotes transposition. For the j -th element of the Tx array, $d_{T,j}$ and $\psi_{T,j}$ are its distance and angle from the Tx array’s reference point as shown in Fig. 1. The position of the j -th element of the Tx array is given by $\mathbf{p}_{T,j} = d_{T,j}\mathbf{u}(\psi_{T,j}) \in \mathbb{R}^2$, $j = 0, \dots, N_T - 1$, where $\mathbf{u}(\psi) = [\cos(\psi), \sin(\psi)]^T$. The Rx

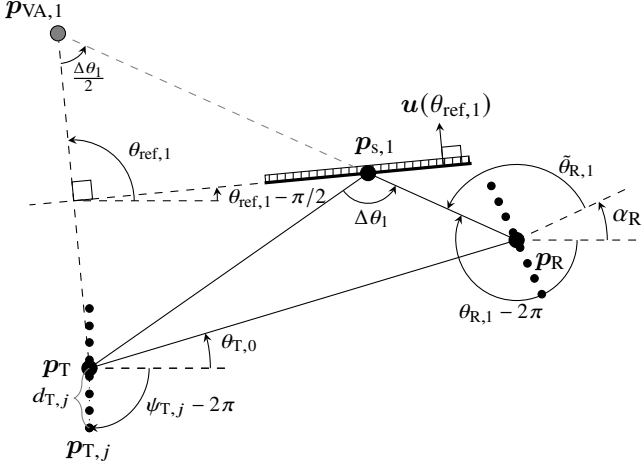


Fig. 1. Geometric model, example with uniform linear arrays (ULAs) at the Tx and the Rx.

consists of an array with N_R antennas, orientation α_R (with respect to the Tx array's orientation) and reference point located at $\mathbf{p}_R = [p_{R,x}, p_{R,y}]^T \in \mathbb{R}^2$. The position of antenna elements at the Rx array are defined similarly as for the Tx. Between each Tx-Rx pair of antennas there are L discrete propagation paths, where the first path ($l = 0$) is the LOS path and the rest ($l = 1, \dots, L-1$) are single-bounce NLOS paths. The l -th single-bounce NLOS path results from a reflection on a flat surface with normal vector $\mathbf{u}(\theta_{\text{ref},l})$ and point of incidence $\mathbf{p}_{s,l} = [p_{s,l,x}, p_{s,l,y}]^T$. Each single-bounce NLOS can be viewed as a direct path resulting from a VA, with the l -th VA located at $\mathbf{p}_{VA,l} = [p_{VA,l,x}, p_{VA,l,y}]^T$, $l = 1, \dots, L-1$. The length of the l -th path is given by d_l , i.e. $d_l = \|\mathbf{p}_R - \mathbf{p}_T\|_2$ for $l = 0$ and $d_l = \|\mathbf{p}_R - \mathbf{p}_{VA,l}\|_2$ for $l \neq 0$, with $\|\cdot\|_2$ being the Euclidean norm. The AOAs are defined as

$$\theta_{R,l} = \begin{cases} \text{atan2}(p_{T,y} - p_{R,y}, p_{T,x} - p_{R,x}), & l = 0, \\ \text{atan2}(p_{VA,l,y} - p_{R,y}, p_{VA,l,x} - p_{R,x}), & l \neq 0, \end{cases} \quad (1)$$

with $\text{atan2}(y, x)$ being the four-quadrant inverse tangent function. The AOAs in the local frame of the Rx are defined as $\tilde{\theta}_{R,l} = \theta_{R,l} - \alpha_R$, $l = 0, \dots, L-1$. With the observation that for a single-bounce reflection it holds that $\theta_{\text{ref},l} = (\theta_{T,l} + \theta_{R,l})/2$, the AODs can be expressed as

$$\theta_{T,l} = \begin{cases} \theta_{R,0} - \pi, & l = 0, \\ 2 \text{atan2}(p_{VA,l,y} - p_{T,y}, p_{VA,l,x} - p_{T,x}) - \theta_{R,l}, & l \neq 0. \end{cases} \quad (2)$$

The array dimensions are much smaller than the distances between Tx, Rx and reflectors. Thus, the delay of the l -th path from Tx element j to Rx element i can be approximated by $\tau_{i,j} \approx \tau_l - \tau_{T,j}(\tilde{\theta}_{T,l}) - \tau_{R,i}(\tilde{\theta}_{R,l})$, where $\tau_{T,j}(\tilde{\theta}_{T,l}) = d_{T,j} \mathbf{u}^T(\psi_{T,j}) \mathbf{u}(\tilde{\theta}_{T,l})/c$, $\tau_{R,i}(\tilde{\theta}_{R,l}) = d_{R,i} \mathbf{u}^T(\psi_{R,i}) \mathbf{u}(\tilde{\theta}_{R,l})/c$ and

$$\tau_l = \begin{cases} (\|\mathbf{p}_R - \mathbf{p}_T\|_2 + d_{\text{clk}})/c, & l = 0 \\ (\|\mathbf{p}_R - \mathbf{p}_{VA,l}\|_2 + d_{\text{clk}})/c, & l \neq 0, \end{cases} \quad (3)$$

where $d_{\text{clk}} = c\epsilon_{\text{clk}}$ with ϵ_{clk} as the clock offset between Tx and Rx and c as the speed of light.

An orthogonal frequency-division multiplexing (OFDM) waveform with N subcarriers and subcarrier spacing Δf is considered. The set of used subcarriers is given by \mathcal{P} . A narrowband signal model is assumed, i.e. $B/f_c \ll \lambda_c/D_{\text{max}}$, where $B \approx \Delta f(\max(\mathcal{P}) - \min(\mathcal{P}))$ is the signal bandwidth, f_c and λ_c are the carrier frequency and wavelength, and D_{max} is the largest dimension of the Tx and Rx arrays. The received signal at the p -th subcarrier (for $p \in \mathcal{P}$) is

$$\mathbf{y}[p] = \mathbf{m}[p] + \boldsymbol{\eta}[p], \quad (4)$$

where $\boldsymbol{\eta}[p] \sim \mathcal{N}_{\mathbb{C}}(\mathbf{0}, \sigma_{\eta}^2 \mathbf{I}_{N_R})$ is the additive white Gaussian noise (AWGN) at the p -th subcarrier and

$$\mathbf{m}[p] = \sum_{l=0}^{L-1} h_l e^{-j\omega_p \tau_l} \mathbf{a}_R(\tilde{\theta}_{R,l}) \mathbf{a}_T^T(\tilde{\theta}_{T,l}) \mathbf{x}[p], \quad (5)$$

where $h_l \in \mathbb{C}$ is the gain of the l -th path, $\omega_p = 2\pi p \Delta f$, and $\mathbf{x}[p] \in \mathbb{C}^{N_T}$ is the reference signal of the p -th subcarrier. With $\omega_c = 2\pi f_c$, the Tx array steering vector $\mathbf{a}_T(\tilde{\theta}_{T,l})$ is given

$$\mathbf{a}_T(\tilde{\theta}_{T,l}) = [e^{j\omega_c \tau_{T,1}(\tilde{\theta}_{T,l})}, \dots, e^{j\omega_c \tau_{T,N_T}(\tilde{\theta}_{T,l})}]^T \in \mathbb{C}^{N_T}, \quad (6)$$

with the Rx steering vector $\mathbf{a}_R(\tilde{\theta}_{R,l})$ defined similarly.

III. CRAMÉR-RAO LOWER BOUND

We first define the channel parameter vector $\boldsymbol{\phi} \in \mathbb{R}^{5L}$ as

$$\boldsymbol{\phi} = [\tau_0, \tilde{\theta}_{T,0}, \tilde{\theta}_{R,0}, \mathbf{h}_0^T, \dots, \tau_{L-1}, \theta_{T,L-1}, \theta_{R,L-1}, \mathbf{h}_{L-1}^T]^T. \quad (7)$$

and the position parameter vector

$$\tilde{\boldsymbol{\phi}} = [\mathbf{p}_R, \alpha_R, d_{\text{clk}}, \mathbf{p}_{VA,1}, \dots, \mathbf{p}_{VA,L-1}]^T \in \mathbb{R}^{2L+2}. \quad (8)$$

According to the Cramér-Rao lower bound (CRLB), the covariance matrix $\mathbf{C}_{\tilde{\boldsymbol{\phi}}}$ of any unbiased estimator $\hat{\tilde{\boldsymbol{\phi}}}$ of $\tilde{\boldsymbol{\phi}}$ satisfies $\mathbf{C}_{\tilde{\boldsymbol{\phi}}} - \mathbf{J}_{\tilde{\boldsymbol{\phi}}}^{-1} \geq \mathbf{0}$ [13], where $\geq \mathbf{0}$ denotes positive semi-definiteness and $\mathbf{J}_{\tilde{\boldsymbol{\phi}}} \in \mathbb{R}^{(2L+2) \times (2L+2)}$ is the hybrid Fisher information matrix (FIM) of $\tilde{\boldsymbol{\phi}}$ given by $\mathbf{J}_{\tilde{\boldsymbol{\phi}}} = \mathbf{J}_{\tilde{\boldsymbol{\phi}}}^{(p)} + \mathbf{J}_{\tilde{\boldsymbol{\phi}}}^{(o)}$, with $\mathbf{J}_{\tilde{\boldsymbol{\phi}}}^{(p)}$ and $\mathbf{J}_{\tilde{\boldsymbol{\phi}}}^{(o)}$ accounting for the prior information and observation-related information on $\tilde{\boldsymbol{\phi}}$, respectively. We note that the hybrid FIM and the corresponding CRLB characterize the estimation performance for a deterministic $\boldsymbol{\phi}$, where two sources of information are used: the received signal and the prior $p(\tilde{\boldsymbol{\phi}})$ [14]. The observation-related FIM $\mathbf{J}_{\tilde{\boldsymbol{\phi}}}^{(o)}$ can be obtained based on the FIM $\mathbf{J}_{\boldsymbol{\phi}}^{(o)}$ of the channel parameter vector $\boldsymbol{\phi}$ as $\mathbf{J}_{\tilde{\boldsymbol{\phi}}}^{(o)} = \mathbf{T} \mathbf{J}_{\boldsymbol{\phi}}^{(o)} \mathbf{T}^T$. The entries of $\mathbf{J}_{\boldsymbol{\phi}}^{(o)} \in \mathbb{R}^{5L \times 5L}$ and $\mathbf{T} \in \mathbb{R}^{2L+2 \times 5L}$ are given by

$$[\mathbf{J}_{\boldsymbol{\phi}}^{(o)}]_{i,j} = \frac{2}{\sigma_{\eta}^2} \sum_{p \in \mathcal{P}} \Re \left\{ \frac{\partial \mathbf{m}^H[p]}{\partial \phi_i} \frac{\partial \mathbf{m}[p]}{\partial \phi_j} \right\}, \quad i, j = 1, \dots, 5L, \quad (9)$$

$$[\mathbf{T}]_{i,j} = \partial \phi_j / \partial \tilde{\phi}_i, \quad i = 1, \dots, 2L+2, \quad j = 1, \dots, 5L, \quad (10)$$

where \mathbf{m}^H is the conjugate transpose of \mathbf{m} and $\Re\{\mathbf{m}\}$ is its real part. Details on the required derivatives can be found in [12]. The position error bound (PEB) for the Rx is defined as

$$\text{Rx PEB} = \sqrt{[\mathbf{J}_{\tilde{\boldsymbol{\phi}}}^{-1}]_{1,1} + [\mathbf{J}_{\tilde{\boldsymbol{\phi}}}^{-1}]_{2,2}} \quad (11)$$

and the PEB for the VAs is defined in a similar manner.

The Rx has prior information on the clock offset $p(\epsilon'_{\text{clk}}) = \mathcal{N}(\epsilon'_{\text{clk}}; \epsilon_{\text{clk}}, \sigma_{\text{clk}}^2)$ and the VAs' locations $p(\mathbf{p}'_{\text{VA},l}) = \mathcal{N}(\mathbf{p}'_{\text{VA},l}; \mathbf{p}_{\text{VA},l}, \Sigma_{\text{VA},\text{pr},l})$, which encode map information about reflectors available at the Rx, with $\mathcal{N}(\mathbf{x}; \boldsymbol{\mu}, \boldsymbol{\Sigma})$ denoting that \mathbf{x} follows a Gaussian distribution with mean $\boldsymbol{\mu}$ and covariance $\boldsymbol{\Sigma}$. The hybrid FIM of the position parameter vector is

$$\mathbf{J}_{\hat{\phi}} = \mathbf{T} \mathbf{J}_{\phi}^{(o)} \mathbf{T}^T + \begin{bmatrix} \mathbf{0} & \mathbf{0} \\ \mathbf{0} & \mathbf{J}_{\text{VA},\text{pr}} \end{bmatrix} + \frac{1}{c\sigma_{\text{clk}}^2} \mathbf{e}_4 \mathbf{e}_4^T, \quad (12)$$

where

$$\mathbf{J}_{\text{VA},\text{pr}} = \begin{bmatrix} \Sigma_{\text{VA},\text{pr},1}^{-1} & & \mathbf{0} \\ & \ddots & \\ \mathbf{0} & & \Sigma_{\text{VA},\text{pr},L-1}^{-1} \end{bmatrix} \in \mathbb{R}^{2(L-1) \times 2(L-1)} \quad (13)$$

where $\Sigma_{\text{VA},\text{pr},l} \in \mathbb{R}^{2 \times 2}$ for $l = 1, \dots, L-1$ is the covariance matrix of the l -th VA's location given by

$$\Sigma_{\text{VA},\text{pr},l} = [\mathbf{u}(\theta_{\text{R},l}) \ \mathbf{u}_{\perp}(\theta_{\text{R},l})] \begin{bmatrix} \sigma_{l,\parallel}^2 & \rho_l \sigma_{l,\parallel} \sigma_{l,\perp} \\ \rho_l \sigma_{l,\parallel} \sigma_{l,\perp} & \sigma_{l,\perp}^2 \end{bmatrix} \begin{bmatrix} \mathbf{u}_{\text{R},l}^T \\ \mathbf{u}_{\perp,\text{R},l}^T \end{bmatrix}, \quad (14)$$

where $\mathbf{u}_{\perp}(\theta) = \mathbf{u}(\theta - \pi/2)$.

We employ the EFIM [15], to focus on the available information on the parameters of interest. Splitting \mathbf{T} as $\mathbf{T} = [\mathbf{T}_{\text{poc}}^T \ \mathbf{T}_{\text{VA}}^T]^T$, with $\mathbf{T}_{\text{poc}} \in \mathbb{R}^{4 \times 5L}$ comprising the first four rows of \mathbf{T} corresponding to the position and orientation parameters and clock offset and $\mathbf{T}_{\text{VA}} \in \mathbb{R}^{2(L-1) \times 5L}$ including the rest of the rows of \mathbf{T} , the EFIM for the position and orientation parameters and clock offset is given by

$$\mathbf{J}_{\text{poc}} = \mathbf{T}_{\text{poc}} \mathbf{J}_{\phi} \mathbf{T}_{\text{poc}}^T - \mathbf{T}_{\text{poc}} \mathbf{J}_{\phi} \mathbf{T}_{\text{VA}}^T \mathbf{J}_{\text{VA}}^{-1} \mathbf{T}_{\text{VA}} \mathbf{J}_{\phi} \mathbf{T}_{\text{poc}}^T + \frac{\mathbf{e}_4 \mathbf{e}_4^T}{(c\sigma_{\text{clk}})^2}, \quad (15)$$

where $\mathbf{J}_{\text{VA}} = \mathbf{T}_{\text{VA}} \mathbf{J}_{\phi} \mathbf{T}_{\text{VA}}^T + \mathbf{J}_{\text{VA},\text{pr}}$.

Making use of the fact that for large bandwidth and number of antennas the paths become asymptotically orthogonal [6], $\mathbf{J}_{\phi}^{(o)}$ becomes a diagonal matrix. Indexing the diagonal elements of $\mathbf{J}_{\phi}^{(o)}$ by the parameter they correspond to, e.g. $J_{\tau_0} = [\mathbf{J}_{\phi}^{(o)}]_{1,1}$, it can be shown that (15) can be written as

$$\mathbf{J}_{\text{poc}} = \frac{J_{\tau_0}}{c^2} \mathbf{z}_{\tau_0} \mathbf{z}_{\tau_0}^T + \frac{J_{\theta_{\text{T},0}}}{d_0^2} \mathbf{z}_{\theta_{\text{T},0}} \mathbf{z}_{\theta_{\text{T},0}}^T + \frac{J_{\theta_{\text{R},0}}}{d_0^2} \mathbf{z}_{\theta_{\text{R},0}} \mathbf{z}_{\theta_{\text{R},0}}^T + \sum_{l=1}^{L-1} \mathbf{J}_l + \frac{\mathbf{e}_4 \mathbf{e}_4^T}{(c\sigma_{\text{clk}})^2}$$

where the EFIM \mathbf{J}_l of the l -th NLOS path is

$$\mathbf{J}_l = \frac{1}{|\mathbf{J}_{\text{VA},l}|} [\mathbf{z}_{\tau_l}, \mathbf{z}_{\theta_{\text{T},l}}, \mathbf{z}_{\theta_{\text{R},l}}] \mathbf{M}_l [\mathbf{z}_{\tau_l}, \mathbf{z}_{\theta_{\text{T},l}}, \mathbf{z}_{\theta_{\text{R},l}}]^T \quad (16)$$

with

$$\mathbf{z}_{\tau_l} = [-\mathbf{u}^T(\theta_{\text{R},l}), \ 0, \ 1]^T \quad (17)$$

$$\mathbf{z}_{\theta_{\text{T},l}} = [\mathbf{u}_{\perp}^T(\theta_{\text{R},l}), \ 0, \ 0]^T \quad (18)$$

$$\mathbf{z}_{\theta_{\text{R},l}} = [\mathbf{u}_{\perp}^T(\theta_{\text{R},l}), \ -d_l, \ 0]^T \quad (19)$$

and $\mathbf{u}_{\perp}(\theta) = \mathbf{u}(\theta - \frac{\pi}{2})$. The entries of $\mathbf{M}_l \in \mathbb{C}^{3 \times 3}$ and $|\mathbf{J}_{\text{VA},l}|$ in (16) are given in the Appendix.

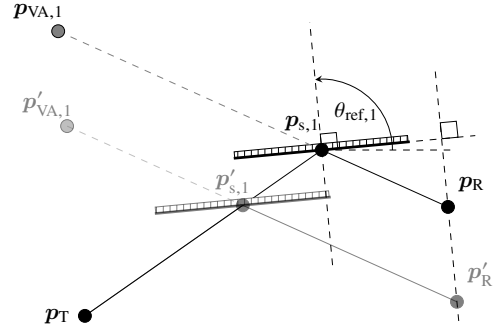


Fig. 2. Potential solutions for p_{R} , $p_{s,l}$ and $p_{\text{VA},l}$ explaining the measurements for a single-bounce reflection.

IV. GEOMETRIC INTERPRETATION OF POSITION INFORMATION

It is interesting to carefully examine and obtain geometric intuition on the position information for the cases of perfect and no knowledge of the VA's position. The former case is straightforward: from (16) for $\sigma_{l,\parallel}, \sigma_{l,\perp} \rightarrow 0$ we get

$$\mathbf{J}_l = \frac{J_{\tau_l}}{c^2} \mathbf{z}_{\tau_l} \mathbf{z}_{\tau_l}^T + \frac{J_{\theta_{\text{T},l}}}{d_l^2} \mathbf{z}_{\theta_{\text{T},l}} \mathbf{z}_{\theta_{\text{T},l}}^T + \frac{J_{\theta_{\text{R},l}}}{d_l^2} \mathbf{z}_{\theta_{\text{R},l}} \mathbf{z}_{\theta_{\text{R},l}}^T. \quad (20)$$

As expected, in this case the NLOS path acts in the same way as LOS path. Using (20) and (17)-(19) we can see that the rank of \mathbf{J}_l is equal to 3, with each of the measurements providing position and orientation information independently: the TOA provides position information in the radial direction, the AOD and AOA provide position information in the tangential direction and the AOA provides orientation information.

In the case of no knowledge of the VA's location, i.e. $\sigma_{l,\parallel}, \sigma_{l,\perp} \rightarrow \infty$, it can be shown that (16) becomes

$$\mathbf{J}_l = j_l \mathbf{z}_l \mathbf{z}_l^T \quad (21)$$

where

$$j_l = \frac{J_{\tau_l} J_{\theta_{\text{T},l}} J_{\theta_{\text{R},l}}}{|\mathbf{J}_{\text{VA},l}| c^2 d_{\text{T},s,l}^2 \cos^2(\Delta\theta_l/2)} \quad (22)$$

$$\mathbf{z}_l = [\mathbf{u}_{\perp}^T(\theta_{\text{ref},l}), \ -d_{\text{R},s,l} \cos(\Delta\theta_l/2), \ \sin(\Delta\theta_l/2)]^T, \quad (23)$$

with $d_{\text{T},s,l} = \|\mathbf{p}_{s,l} - \mathbf{p}_{\text{T}}\|_2$ and $d_{\text{R},s,l} = \|\mathbf{p}_{\text{R}} - \mathbf{p}_{s,l}\|_2$. We can observe from (21) that, as first noted in [11], \mathbf{J}_l has rank 1. Furthermore, from (23) and Fig. 1, we conclude that the direction of position information is always parallel to the reflecting surface and independent of the Tx and Rx location. At first glance, this is a surprising result, since for LOS paths and NLOS paths with perfect knowledge of the corresponding VAs' location the direction of position information depends on \mathbf{p}_{R} and \mathbf{p}_{T} . A geometrically intuitive explanation of this result can be obtained from Fig. 2. In Fig. 2 we consider a single-bounce reflection and plot two potential geometries $\{\mathbf{p}_{\text{R}}, \mathbf{p}_{s,1}, \mathbf{p}_{\text{VA},1}\}$ and $\{\mathbf{p}'_{\text{R}}, \mathbf{p}'_{s,1}, \mathbf{p}'_{\text{VA},1}\}$ that would produce the same TOA, AOD and AOA. In fact, there are infinitely many such geometries, parametrized as

$$\mathbf{p}_{\text{R}} = \mathbf{p}_{\text{T}} - c \cdot \tau_l \mathbf{u}(\theta_{\text{R},l}) + 2\lambda \cos(\Delta\theta_l/2) \mathbf{u}(\theta_{\text{ref},l}) \quad (24)$$

$$\mathbf{p}_{\text{VA},l} = \mathbf{p}_{\text{T}} + 2\lambda \cos(\Delta\theta_l/2) \mathbf{u}(\theta_{\text{ref},l}) \quad (25)$$

$$\mathbf{p}_{s,l} = \mathbf{p}_{\text{T}} + \lambda \mathbf{u}(\theta_{\text{T},l}), \quad (26)$$

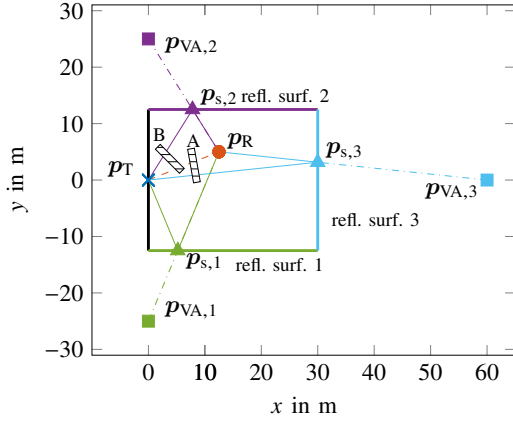


Fig. 3. Simulation scenario.

with $0 < \lambda < c \cdot \tau_l$. As can be seen in (24), the locus of \mathbf{p}_R is a line segment normal to the reflecting surface. Hence, the NLOS path associated with the reflection provides position information only in the direction that is perpendicular to this line segment, i.e. in the direction parallel to the reflecting surface. An implication of this result is that information from single-bounce paths from parallel (or close to parallel) reflecting surfaces may not suffice for target localization.

V. NUMERICAL RESULTS

A. Simulation setup

We set $f_c = 38$ GHz, $N = 1024$, $\Delta f = 120$ kHz, $\mathcal{P} = \{-420, \dots, -1, 1, \dots, 420\}$ and $B \approx 100$ MHz. The entries of $\mathbf{x}[p]$ have constant amplitude and random phase, with $E[\|\mathbf{x}[p]\|_2^2] = 0$ dBm. The noise variance is $\sigma_\eta^2 = 10^{0.1(n_{\text{Rx}} + N_0)} N \Delta f$, where $N_0 = -174$ dBm Hz⁻¹ is the noise power spectral density and $n_{\text{Rx}} = 8$ dB is the Rx noise figure.

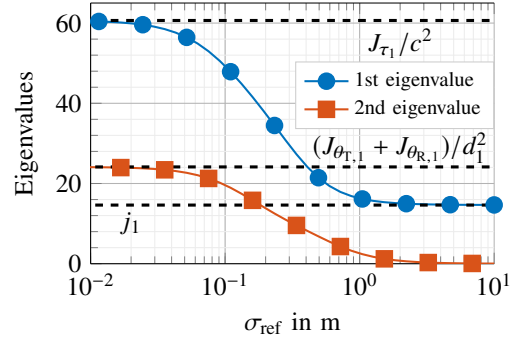
We consider the scenario depicted in Fig. 3, where the Tx lies at the origin and the Rx at $\mathbf{p}_R = [12.5, 5]^T$ m. The Tx has a ULA with 32 antennas and the Rx has a UCA with 16 antennas and orientation α_R . The VAs resulting from single-bounce reflections at the rooms' walls are located at $p_{\text{VA},1} = [0, -25]^T$ m, $p_{\text{VA},2} = [0, 25]^T$ m and $p_{\text{VA},3} = [60, 0]^T$ m. In order to concentrate on the potential implications of the results presented in Sec. IV, we assume that the Rx orientation α_R is known and the Tx and Rx are perfectly synchronized. We consider two NLOS-only cases:

- *case A*: the paths corresponding to the 1st and 2nd VAs are received;
- *case B*: the paths corresponding to the 1st and 3rd VAs are received.

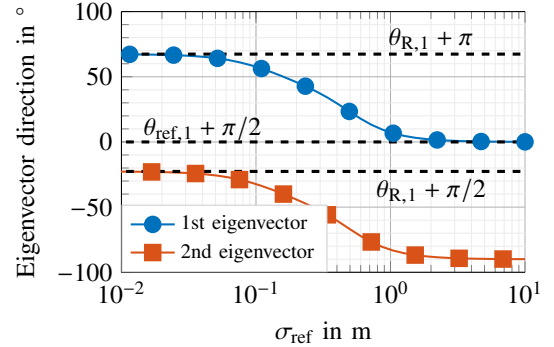
The amplitude of the complex path gain of the l -th path is $|h_l| = \sqrt{\gamma_l \lambda / (4\pi d_l)}$, where $\gamma_l = 0.1 \forall l$, is the reflection coefficient, and the phase is uniformly distributed.

B. Results

From the analysis in Sec. IV we have a clear picture about the position information offered by single-bounce NLOS paths under perfect or no prior knowledge of their corresponding



(a) Eigenvalues of \mathbf{J}_1 .



(b) Direction eigenvectors of \mathbf{J}_1 .

Fig. 4. Eigenvalues and directions of eigenvectors of the EFIM \mathbf{J}_1 of VA 1 as function of the prior VA position error σ_{ref} .

VAs locations. In order to gain more insight about the intermediate cases, setting $\rho_l = 0$ and $\sigma_{l,\parallel} = \sigma_{l,\perp} = \sigma_{\text{ref}}/\sqrt{2}$, we plot the eigenvalues and the directions of the eigenvectors for varying σ_{ref} in Fig. 4. We see that, as expected, when knowledge about the VA's position is accurate ($\sigma_{\text{ref}} \rightarrow 0$), for known orientation and perfect synchronization (in this case $\mathbf{z}_{\theta_{r,l}} = \mathbf{z}_{\theta_{R,l}} = \mathbf{u}_\perp^T(\theta_{R,l})$), \mathbf{J}_1 has two strong eigenvalues, with the eigenvectors pointing in the radial and the tangential direction. As σ_{ref} increases, the strongest eigenvalue decreases, starting from J_{τ_1}/c^2 and converges to j_1 , while the second eigenvalue vanishes, resulting in a rank-1 \mathbf{J}_1 . The direction of the eigenvector corresponding to the strongest eigenvalue gradually changes from $\theta_{R,1} + \pi$, which corresponds to range information, to $\theta_{\text{ref},1} + \pi/2$, that is parallel to the reflecting surface.

In Fig. 5 we plot the PEB of the Rx and VA 1 for the two considered cases as functions of σ_{ref} . We set again $\rho_l = 0$ and $\sigma_{l,\parallel} = \sigma_{l,\perp} = \sigma_{\text{ref}}/\sqrt{2}$, $l = 1, 2, 3$. We see that for $\sigma_{\text{ref}} \rightarrow 0$ the PEB of VA 1 converges to 0, while the Rx PEB converges to its lowest value as the two paths behave as LOS paths, providing position information in linearly independent directions. In case A, as σ_{ref} increases the two paths provide position information in almost the same direction, as they arise from parallel reflecting surfaces, with the available information in the orthogonal direction decreasing with increasing σ_{ref} . As a result, for high values of σ_{ref} (i.e. less accurate prior) the PEB of the Rx and VA 1 grows linearly with σ_{ref} . In case A, for high values of σ_{ref} (i.e. less accurate prior) the PEB of the Rx and VA 1 grows linearly with σ_{ref} . This is due to the fact that

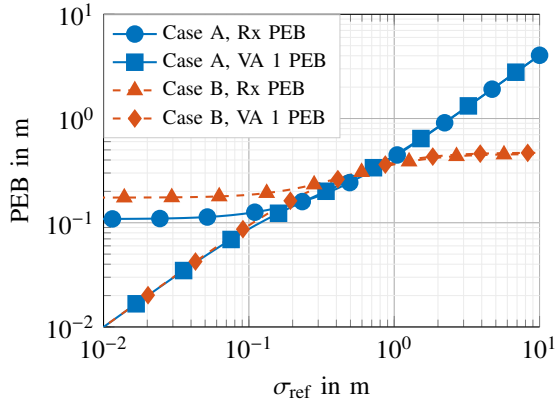


Fig. 5. Rx and VA 1 PEB as function of the prior VA position error σ_{ref} .

the two paths provide position information in almost the same direction, as they arise from parallel reflecting surfaces, with the available information in the orthogonal direction decreasing with increasing σ_{ref} . For moderate values of σ_{ref} (< 1 m), good positioning accuracy is achievable as, the directions of the strongest eigenvectors of \mathbf{J}_1 and \mathbf{J}_2 are sufficiently distinct. On the contrary, in case B, the PEB of the Rx and VA 1 saturates for high values of σ_{ref} , as the two paths provide position information in different directions, resulting from the two perpendicular walls. Therefore, combining the two NLOS paths the Rx position can be resolved and, consequently, the position of the VA.

VI. CONCLUSION

We provided an analysis of the Fisher information on position, orientation and clock offset provided by single-bounce NLOS paths. The effect of prior map information on the position information was studied. It was shown that when no prior knowledge is available, the direction of position information is always parallel to the reflecting surface, independent of the Rx target position. We also provided a geometrically intuitive explanation of the result. Numerical examples considering a practical room geometry showed that, as a consequence of the aforementioned analysis, the availability of different multipath components can have a significant impact on the achievable positioning accuracy.

APPENDIX

ENTRIES OF \mathbf{M}_l AND $|\mathbf{J}_{\text{VA},l}|$ IN (16)

The entries of \mathbf{M}_l and $|\mathbf{J}_{\text{VA},l}|$ in (16) are given by

$$[\mathbf{M}_l]_{1,1} = \frac{J_{\tau_l}}{c^2} J_{\theta_{\tau,l}} A^2 F + \frac{1}{(1-\rho_l^2)\sigma_{l,\parallel}^2} \left(J_{\theta_{\tau,l}} B^2 + \frac{J_{\theta_{R,l}}}{d_l^2} + \frac{G}{\sigma_{l,\perp}^2} \right)$$

$$[\mathbf{M}_l]_{2,2} = \frac{J_{\theta_{\tau,l}}}{d_l^2} \left(\frac{J_{\tau_l}}{c^2} F + \frac{1}{(1-\rho_l^2)\sigma_{l,\parallel}^2} P \right)$$

$$[\mathbf{M}_l]_{3,3} = \frac{J_{\theta_{R,l}}}{d_l^2} \left(J_{\theta_{\tau,l}} B^2 Q + \frac{1}{(1-\rho_l^2)\sigma_{l,\perp}^2} \left(\frac{J_{\tau_l}}{c^2} + J_{\theta_{\tau,l}} A + \frac{G}{\sigma_{l,\parallel}^2} \right) \right)$$

$$[\mathbf{M}_l]_{1,2} = [\mathbf{M}_l]_{2,1} = \frac{J_{\tau_l}}{c^2} \frac{J_{\theta_{\tau,l}}}{d_l} \left(AF + B \frac{\rho_l}{(1-\rho_l^2)\sigma_{l,\parallel}^2 \sigma_{l,\perp}^2} \right)$$

$$[\mathbf{M}_l]_{1,3} = [\mathbf{M}_l]_{3,1} = \frac{J_{\tau_l}}{c^2} \frac{J_{\theta_{\tau,l}}}{d_l^2} \left(\frac{\rho_l}{(1-\rho_l^2)\sigma_{l,\parallel}^2 \sigma_{l,\perp}^2} - J_{\theta_{\tau,l}} AB \right)$$

$$[\mathbf{M}_l]_{2,3} = [\mathbf{M}_l]_{3,2} = \frac{J_{\theta_{\tau,l}}}{d_l} \frac{J_{\theta_{R,l}}}{d_l^2} \left(BQ + \frac{A\rho_l}{(1-\rho_l^2)\sigma_{l,\parallel}^2 \sigma_{l,\perp}^2} \right)$$

$$|\mathbf{J}_{\text{VA},l}| = \frac{J_{\tau_l}}{c^2} (J_{\theta_{\tau,l}} B^2 + F) + \frac{P + J_{\theta_{\tau,l}} B(B + 2\rho_l A \sigma_{l,\parallel} / \sigma_{l,\perp})}{(1-\rho_l^2)\sigma_{l,\parallel}^2} + J_{\theta_{\tau,l}} A^2 F,$$

where $A = \tan(\frac{\Delta\theta_l}{2})/d_{\text{T},s,l}$, $B = 1/d_l - 1/d_{\text{T},s,l}$, $\Delta\theta_l = \theta_{R,l} - \theta_{\tau,l}$, $F = \frac{J_{\theta_{R,l}}}{d_l^2} + \frac{1}{(1-\rho_l^2)\sigma_{l,\perp}^2}$, $G = 1 + 2\rho_l \sigma_{l,\parallel} \sigma_{l,\perp} J_{\theta_{\tau,l}} AB$, $P = \frac{J_{\theta_{R,l}}}{d_l^2} + \frac{1}{\sigma_{l,\perp}^2}$ and $Q = \frac{J_{\tau_l}}{c^2} + \frac{1}{(1-\rho_l^2)\sigma_{l,\parallel}^2}$.

REFERENCES

- [1] Li Cong and Weihua Zhuang, "Nonline-of-sight error mitigation in mobile location," *IEEE Trans. Wireless Commun.*, vol. 4, no. 2, pp. 560–573, Mar. 2005.
- [2] S. Marano, W. M. Gifford, H. Wymeersch, and M. Z. Win, "NLOS identification and mitigation for localization based on UWB experimental data," *IEEE J. Sel. Areas Commun.*, vol. 28, no. 7, pp. 1026–1035, Aug. 2010.
- [3] H. Miao, K. Yu, and M. J. Juntti, "Positioning for NLOS propagation: Algorithm derivations and Cramér–Rao bounds," *IEEE Trans. Veh. Technol.*, vol. 56, no. 5, pp. 2568–2580, Sep. 2007.
- [4] K. Papakostantinou and D. Slock, "NLOS mobile terminal position and speed estimation," in *3rd Int. Symposium on Commun., Control and Signal Process.*, St Julians, Malta, Mar. 2008, pp. 1308–1313.
- [5] K. Witrals, P. Meissner, E. Leitinger, Y. Shen, C. Gustafson, F. Tufveson, K. Haneda, D. Dardari, A. F. Molisch, A. Conti, and M. Z. Win, "High-accuracy localization for assisted living: 5G systems will turn multipath channels from foe to friend," *IEEE Signal Process. Mag.*, vol. 33, no. 2, pp. 59–70, Mar. 2016.
- [6] Z. Abu-Shaban, X. Zhou, T. D. Abhayapala, G. Seco-Granados, and H. Wymeersch, "Error bounds for uplink and downlink 3D localization in 5G mmWave systems," *IEEE Trans. Wireless Commun.*, vol. 17, no. 8, pp. 4939–4954, Aug. 2018.
- [7] A. Shahmansoori, G. E. Garcia, G. Destino, G. Seco-Granados, and H. Wymeersch, "5G position and orientation estimation through millimeter wave MIMO," in *Proc. IEEE GLOBECOM Workshops (GC Wkshps)*, San Diego, CA, Dec. 2015, pp. 1–6.
- [8] —, "Position and orientation estimation through millimeter-wave MIMO in 5G systems," *IEEE Trans. Wireless Commun.*, vol. 17, no. 3, pp. 1822–1835, Mar. 2018.
- [9] R. Mendrzik, H. Wymeersch, and G. Bauch, "Joint localization and mapping through millimeter wave MIMO in 5G systems," in *Proc. IEEE Global Commun. Conf. (GLOBECOM)*, Abu Dhabi, UAE, 2018, pp. 1–6.
- [10] J. Talvitie, M. Koivisto, T. Levanen, M. Valkama, G. Destino, and H. Wymeersch, "High-accuracy joint position and orientation estimation in sparse 5G mmWave channel," in *Proc. IEEE Int. Conf. Commun. (ICC)*, Shanghai, China, May 2019, pp. 1–7.
- [11] R. Mendrzik, H. Wymeersch, G. Bauch, and Z. Abu-Shaban, "Harnessing NLOS components for position and orientation estimation in 5G millimeter wave MIMO," *IEEE Trans. Wireless Commun.*, vol. 18, no. 1, pp. 93–107, Jan. 2019.
- [12] A. Kakkavas, M. H. Castañeda García, R. A. Stirling-Gallacher, and J. A. Nassek, "Performance limits of single-anchor millimeter-wave positioning," *IEEE Trans. Wireless Commun.*, vol. 18, no. 11, pp. 5196–5210, Nov. 2019.
- [13] H. L. Van Trees and K. L. Bell, *Detection, Estimation and Modulation Theory, Part I: Detection, Estimation, and Filtering Theory*, 2nd ed. John Wiley & Sons, 2013.
- [14] H. Wymeersch, N. Garcia, H. Kim, G. Seco-Granados, S. Kim, F. Wen, and M. Fröhle, "5G mmWave downlink vehicular positioning," in *Proc. IEEE Global Commun. Conf. (GLOBECOM)*, Abu Dhabi, UAE, Dec. 2018, pp. 206–212.
- [15] Y. Shen and M. Z. Win, "Fundamental limits of wideband localization accuracy via Fisher information," in *Proc. IEEE Wireless Commun. Netw. Conf. (WCNC)*, Kowloon, Hong Kong, Mar. 2007, pp. 3046–3051.